Transactions of Tianjin University (2019) 25:169–184
https://doi.org/10.1007/s12209-018-0156-4

RESEARCH ARTICLE

Preparation of CeO_2-Modified Mg(Al)O-Supported Pt–Cu Alloy Catalysts Derived from Hydrotalcite-Like Precursors and Their Catalytic Behavior for Direct Dehydrogenation of Propane

Yingxia Li[1,2] · Jiaxin Li[1,2] · Xiao Yang[1,2] · Xitao Wang[1] · Yanhong Xu[3] · Lihong Zhang[1,2]

Received: 11 March 2018 / Revised: 25 April 2018 / Accepted: 28 April 2018 / Published online: 14 May 2018

Abstract
A series of PtCuCeMgAl quintuple hydrotalcite-like compounds with different Ce contents were synthesized by one-pot method. After calcining and reduction, CeO_2-modified Mg(Al)O-supported Pt–Cu alloy catalysts were obtained. To understand the effect of Cu and Ce, the structure and physico-chemistry properties of the catalysts were characterized and analyzed, and the catalytic behaviors were investigated in a direct dehydrogenation of propane to propene. The results show that the Pt^{4+}, Cu^{2+}, and Ce^{3+} ions can be incorporated into the brucite-like layers and the Ce content significantly affects the interaction strength between Pt and Cu and the dehydrogenation performance of propane. Under the reaction conditions, the highest propane conversion (45%) with 89% selectivity to propene and a 40% propene yield were achieved with a 0.3 wt% Ce-modified PtCu/Mg(Al)O catalyst. The improved catalytic performance is related to the easy formation of Pt–Cu alloy phase, excellent resistance to sintering, and coke deposits of active components modified by CeO_2.

Keywords Ce modification · Pt–Cu alloy · Propane dehydrogenation · High dispersion · Anti-sintering

Introduction

Light olefins are important raw materials for producing various chemicals, especially propene is one of the most significant building blocks for polypropylene, propylene oxide, and acrylonitrile, etc. [1]. Propene is mainly produced by steam cracking of naphtha and as a by-product of the fluid catalytic cracking of crude oil. The speed of its production cannot meet its increasing demand, especially with the emergence of many new industries. Hence, a more effective and economical approach of propene production has to be developed. In recent years, propane dehydrogenation (PDH) has been considered as one of the most promising alternatives because of its low-cost and easily obtainable materials [2, 3]. However, PDH is a highly endothermic and equilibrium-limited reaction, which usually requires a high reaction temperature of over 550 °C to obtain high yield [4]. Under such harsh reaction conditions, undesirable side reactions such as thermal cracking, hydrogenolysis, and isomerization can occur, which generates lighter hydrocarbons and serious coke deposits, resulting in rapid catalyst deactivation [5]. Hence, it is highly important to develop catalytic materials that possess excellent anti-coking ability, high propene selectivity, and high propane conversion.

Platinum-based catalysts have been widely utilized in PDH processes because of their high catalytic activity, thermal stability, and eco-friendliness; however, they are not very efficient because of their significant deactivation, which results from coke formation [6, 7] and sintering of active sites [4], and their low propene selectivity, which results from C–C bond cleavage [8].

To obtain optimal performance, some promoters, such as Sn, Ga, In, Zn, Cu, and Na, are added to improve the properties of Pt-based catalysts in PDH reactions [9–11]. In commercial PDH processes, Pt–Sn catalysts supported on Al_2O_3 have been extensively used because of their excellent olefin selectivity and catalytic stability [12, 13]. Although the catalysts have substantial improvements,

✉ Lihong Zhang
zlh_224@163.com

[1] School of Chemical Engineering and Technology, Tianjin University, Tianjin 300350, China

[2] Tianjin Key Laboratory of Applied Catalysis Science and Technology, Tianjin University, Tianjin 300350, China

[3] Department of Materials Engineering, Xuzhou College of Industrial Technology, Xuzhou 221140, China

they still possess limited stability and regenerability. Recently, Zn-doped Pt catalyst has been reported to have an enhanced catalytic performance. For example, a Pt–Zn/Al_2O_3 catalyst can enhance anti-coking ability as well as propene selectivity [14]. Because of their remarkably high activity, selectivity, and stability, Pt–In and Pt–Ga-supported catalysts have also been widely studied [7, 15].

It has been reported that Cu addition can promote catalytic activities of Pt-based catalysts for light hydrocarbon dehydrogenation by forming Pt–Cu alloy [8, 10]. The promoter Cu can suppress coke deposits formation and hydrocarbon cracking, because the intimate interaction of Pt and Cu can inhibit propene adsorption and increase the energy barrier of C–C bond breakage. Han et al. [10] demonstrated that propene selectivity of Pt/Al_2O_3 catalyst increased from 77.2 to 90.8% after Cu addition, although catalyst dispersion slightly decreased because a fraction of Pt surface was covered by Cu. Veldurthi et al. [16] studied Cu-modified Pd/Al_2O_3 and Pt/Al_2O_3 catalysts for n-butane dehydrogenation and reported a superior n-butane conversion, C_4 olefin selectivity, and catalytic stability.

Cerium has been widely applied in several catalytic processes such as steam reforming [17], CO oxidation [18], NO_x reduction [19], and water gas shift [20]. Cerium (IV) oxide has a high oxygen storage capacity and can suppress coke formation by oxidizing carbon deposition on the surface of a catalyst utilizing released lattice oxygen [21]. According to Zhang et al. [22], Pt–Sn/ZSM-5 catalysts modified by Ce can depress coke deposition, stabilize Pt nanoparticles, and strengthen the interaction between Sn species and support, which would result in a high reaction activity, stability, and propene selectivity. Furthermore, it has been proposed that the presence of Ce over Pt-based catalysts can suppress Pt sintering by the intimate interaction of Pt and CeO_x [4].

In addition, it is generally believed that the support does not only affect the catalytic performance of the dehydrogenation reaction, but also influences the properties of the final metal phase [23, 24]. Previous studies indicate that metal oxide supports, such as K-L zeolite, alkali-doped alumina, spinels, and calcined hydrotalcite (HT), can greatly suppress coke formation because of the free acid sites as well as low alkene adsorption [15]. Studies on calcined HT (Mg(Al)O) or HT-like materials are particularly interesting owing to their suitable basic characteristics and high thermal stability. In addition, the surface Al^{3+} ions can effectively enhance the dispersion of metal particles [9, 25]. Akporiaye et al. [26] found that PtSn/Mg(Al)O catalysts showed advanced activity and stability in a PDH reaction compared to PtSn/Al_2O_3 prepared by conventional method. In recent years, it has been reported that Pt/Mg(In)(Al)O and Pt/Mg(Ga)(Al)O catalysts with calcined HT supports exhibit good catalytic activity and alkene selectivity [27, 28].

This study aims to optimize the catalytic activity and anti-sintering of Mg(Al)O-supported Pt-based catalysts in PDH reactions by adding Cu, changing the Ce content, and using a more effective preparation method. The relationship between catalytic performance and the structural features of a series of CeO_2-modified Pt–Cu/Mg(Al)O catalysts was systematically investigated by complementary characterization techniques.

Experimental Details

Preparation of Catalysts

Materials

All reagents used in this study are analytical grade. The chemicals $H_2PtCl_6{\cdot}6H_2O$, $Al(NO_3)_3{\cdot}9H_2O$, $Cu(NO_3)_2{\cdot}3H_2O$, $NaCO_3$, and NaOH were purchased from Tianjin Yuanli Chemical Co. Ltd, and $Mg(NO_3)_2{\cdot}6H_2O$ was purchased from Shanghai Aladdin Biochemical Technology Co. Ltd. Chemical $Ce(NO_3)_3{\cdot}6H_2O$ was purchased from Tianjin Guangfu Fine Chemical Research Institute.

Preparation of PtCu/Ce_xMgAl-R

A series of catalysts were prepared by one-pot synthesis, where 19.23 g of $Mg(NO_3)_2{\cdot}6H_2O$, 9.38 g $Al(NO_3)_3{\cdot}9H_2O$, 1.55 g $Cu(NO_3)_2{\cdot}3H_2O$, 7.23 mL H_2PtCl_6 aqueous solution (19.3 mmol L^{-1}), and a certain amount of $Ce(NO_3)_3{\cdot}6H_2O$ were dissolved in 300 mL of deionized water under magnetic stirring at 90 °C for 10 min. Then, a mixed solution of NaOH and $NaCO_3$, with a CO_3^{2-}/Al^{3+} molar ratio of 2 and $OH^-/(2\ Mg^{2+} + 3Al^{3+})$ molar ratio of 1.6, was added dropwise to the above solution under vigorous stirring until a pH value of 9.7 was achieved. The formed solution was kept at 90 °C for 6 h, and the precipitate was filtered, washed with deionized water, and dried at 80 °C for 24 h. The obtained precursors (marked as PtCuCe_xMgAl-P) were calcined at 550 °C for 4 h to obtain Mg(Pt)(Cu)$(Ce)_x$(Al)O catalysts (marked as PtCuCe_xMgAl-O). Similarly, MgAl-O, PtMgAl-O, $Ce_{3.0}$MgAl-O, CuMgAl-O, PtCuMgAl-O, $PtCe_{3.0}$MgAl-O, and their calcined products were also prepared. For all samples, the loadings of Pt and Cu were fixed at 0.6 and 9.0 wt%, respectively. The content of Ce was changed from 0 to 3.0 wt% by varying the amount of $Ce(NO_3)_3{\cdot}6H_2O$ during the preparation. Prior to the activity test, the sample was reduced in 5 vol% H_2/N_2, which is denoted as PtCu/Ce_xMgAl-R.

For comparison, imp-PtCu/MgAl-O was prepared by conventional sequential impregnation method and calcination. First, Cu^{2+} ion was loaded by incipient wetness impregnation of the as-prepared Mg(Al)O support using $Cu(NO_3)_2{\cdot}3H_2O$

aqueous solution, which was left to stand for 6 h at ambient temperature. After drying at 50 °C for 2 h and 120 °C for 3 h, the sample was calcined at 550 °C for 4 h in a muffle furnace, and Pt was supported on the calcined product by the same procedure as Cu impregnation using $H_2PtCl_6{\cdot}6H_2O$ as precursor. Prior to the activity test, the sample was reduced in 5 vol% H_2/N_2, which is denoted as imp-PtCu/MgAl-R.

Characterization

The X-ray diffraction (XRD) patterns were recorded on a D8-Focus (Bruker) equipped with Cu Kα radiation ($\lambda = 0.15418$ nm). The catalysts were scanned from the 2θ value of 5°–90°, with a scanning speed of 8° min^{-1}. The X-ray tube was manipulated at 40 kV and 40 mA.

The textural properties of the samples were measured by N_2 adsorption–desorption at − 196 °C. Prior to the experiments, the samples were degassed for 4 h at 300 °C. The specific surface areas of the samples were determined by the Brunaure–Emmett–Teller (BET) method. The Barrett–Joyner–Halenda (BJH) method was used to calculate the cumulative pore volume and average pore diameter in accordance with the desorption branches of the isotherms.

The transmission electron microscopy (TEM) images were taken with a JEM-2100F microscope operated at 200 kV. The as-synthesized catalysts were pre-reduced at 580 °C in a flow of 5 vol% H_2/N_2 for 2 h. Then, the samples were dispersed, sonicated in ethanol, and dropped on carbon-film coated copper grids.

Temperature-programmed reduction (TPR) experiments were carried out in a programmable temperature system, and prior to the experiment the baseline was stabilized for 30 min. A H_2-TPR was implemented in 5 vol% H_2/N_2 (30 mL min^{-1}) with a heating rate of 10 °C min^{-1} from room temperature to 850 °C. The H_2 consumption profile was recorded with a thermal conductivity detector.

X-ray photoelectron spectroscopy (XPS) was carried out on a Perkin-Elmer PHI 5000C ESCA using Al Kα radiation. Prior to the analysis, the sample was reduced under 5 vol% H_2/N_2 (30 mL min^{-1}) at 580 °C for 2 h, and the binding energies were calibrated using the C 1 s peak at 284.8 eV as an internal standard.

Thermogravimetric (TG) analysis was carried out with a DTG-50/50H thermal analyzer to determine the quantity of coke on the used catalyst and the TG curves were recorded from room temperature to 900 °C at an increasing rate of 10 °C min^{-1}.

The elemental composition of the samples was analyzed by inductively coupled plasma-optical emission spectroscopy (ICP-OES) using VISTA-MPX.

Dispersion of metals was determined by CO chemisorption. For a fresh catalyst, 100 mg of sample was pre-reduced with H_2 at 580 °C for 1 h and then flushed with Ar flow at 580 °C for 0.5 h. CO chemisorption was carried out at 30 °C by injecting pulses of CO (50 μL) every 3 min until the peak area became stable. The adsorption capacity of CO is calculated by the following equation:

$$\text{CO uptake } (\mu\text{mol } g_{cat}^{-1}) = \frac{n \times A - B}{A} \times \frac{50}{22.4} \times 10, \quad (1)$$

where n stands for the number of chemical adsorption peaks, A represents the average value of the peak area when the peak area remains constant, and B stands for the total area of the chemical adsorption peak.

Activity Test for Propane Dehydrogenation

Activity tests were carried out in a fix-bed reactor with an 8 mm inner diameter. Prior to reaction, 0.4 g sample was reduced in 5 vol% H_2/N_2 (30 mL min^{-1}) at 580 °C for 2 h. Then, a mixture of C_3H_8, H_2 and N_2 with a molar ratio of 8:7:35 was introduced into the reactor and the total flow was 55 mL min^{-1}. The weight hourly space velocity (WHSV) of propane was about 3 h^{-1}. The PDH reaction was performed at atmospheric pressure and 600 °C. The reaction products were analyzed by an online gas chromatograph, equipped with an FID detector and Al_2O_3 column. The catalytic performance of the catalyst was evaluated by C_3H_8 conversion, C_3H_6 selectivity, and C_3H_6 yield, which are calculated by the following equations:

$$\text{Conversion } (\%) = \frac{\sum_i n_i}{\sum_i n_i + \left(n_{C_3H_8}\right)_{out}} \times 100 \quad (2)$$

$$\text{Selectivity } (\%) = \frac{n_i}{\sum_i n_i} \times 100 \quad (3)$$

$$\text{Yield } (\%) = \text{Conversion} \times \text{Selectivity} \times 100, \quad (4)$$

where i stands for the hydrocarbon products in the effluent gas stream, n_i represents the number of carbon atoms of ingredient i, and $\left(n_{C_3H_8}\right)_{out}$ stands for the number of carbon atoms of propane in the effluent gas stream, i.e., unreacted propane during the PDH reaction.

Results and Discussion

Structure of the Precursors

The XRD patterns of the as-synthesized samples with different compositions are shown in Fig. 1. All the precursors display a similar pattern to the typical HT material reported in previous papers [21, 29]. For MgAl-P, PtMgAl-P, CuMgAl-P, PtCuMgAl-P, and PtCuCe$_x$MgAl-P ($x = 0.1$, 0.3) samples, only an HT phase (JCPDS file No. 14-0191) can be observed.

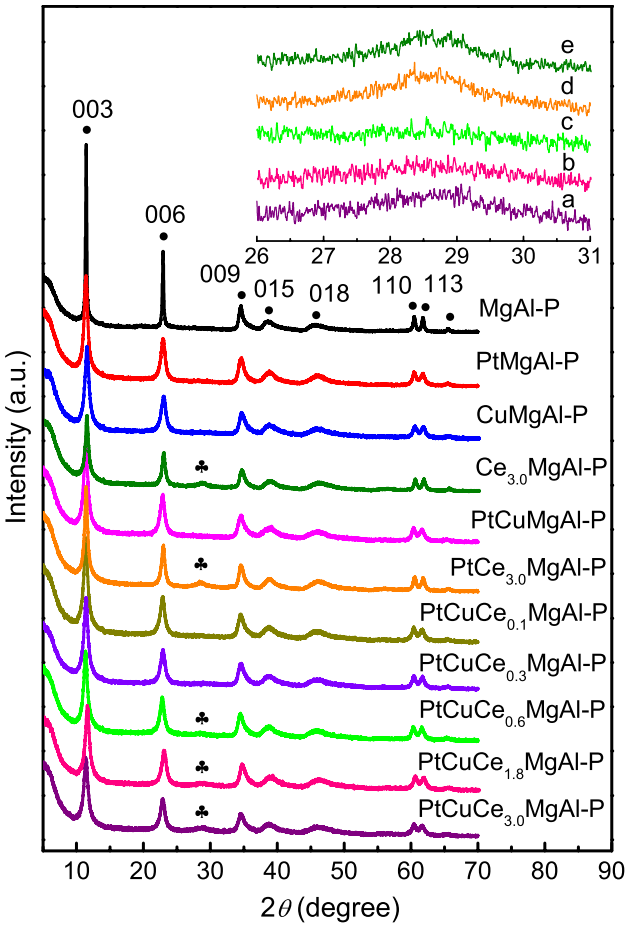

Fig. 1 XRD patterns of the precursors. (black circle) hydrotalcite phase; (black Club) $Ce(OH)_3$. (inset: a. $PtCuCe_{3.0}MgAl$-P; b. $PtCuCe_{1.8}MgAl$-P; c. $PtCuCe_{0.6}MgAl$-P; d. $PtCe_{3.0}MgAl$-P; e. $Ce_{3.0}MgAl$-P)

However, other non-HT phases, such as $Ce(OH)_3$ phase [21], can be indexed at 28.2° in $Ce_{3.0}MgAl$-P, $PtCe_{3.0}MgAl$-P, and $PtCuCe_xMgAl$-P samples with a relatively high Ce content ($x = 0.6$, 1.8, 3.0). This is attributed to the larger ionic radius of Ce^{3+} (0.101 nm) [30] in comparison to that of Al^{3+} (0.054 nm) [30] in the octahedral coordination [21, 29, 31], which can influence the stability of brucite-like layers and even result in the segregation of partial Ce^{3+} ions into non-HT phases for higher Ce-containing samples [21]. The diffraction peaks of the HT phases broaden and weaken with the successive incorporation of Pt, Cu, and Ce ions, reflecting the decrease in crystallinity of the HT phase and shrinkage in crystallite size.

The calculated lattice parameters of the precursors are listed in Table 1. The *a* values of CuMgAl-P, $Ce_{3.0}MgAl$-P, and $PtCuCe_xMgAl$-P samples increase compared to that of MgAl-P. Additionally, the presence of small amounts of Ce^{3+} ions gives rise to an increasing value of lattice parameter *a* across $PtCuCe_{0.1}MgAl$-P, $PtCuCe_{0.3}MgAl$-P, and $PtCuCe_{0.6}MgAl$-P, followed by a decrease with further increase in the Ce content. For CuMgAl-P, the octahedron becomes larger because of the decrease of positive charge density in the layers incorporated with Cu^{2+} ions. As for the Ce-containing samples, it is mainly because Ce^{3+} ions have a bigger radius than Al^{3+} ions, which can broaden the distance between metal cations in the layers and increase the *a* value [31]. The corresponding lattice parameter *c* exhibits a similar trend. Although the reasons are different, it can be confirmed that Cu^{2+} and Ce^{3+} ions can be introduced in the HT structure layers as the amounts of Cu^{2+} and Ce^{3+} ions are small.

Table 1 Lattice parameters of the as-synthesized precursors

Sample	Lattice parameter of HTs (nm)		Crystallite size of HTs (nm)[c]
	a[a]	c[b]	
MgAl-P	0.3060	2.3273	40.6
PtMgAl-P	0.3061	2.3330	11.8
CuMgAl-P	0.3068	2.3404	11.3
$Ce_{3.0}MgAl$-P	0.3064	2.3368	12.9
PtCuMgAl-P	0.3067	2.3329	10.1
$PtCe_{3.0}MgAl$-P	0.3059	2.3308	13.3
$PtCuCe_{0.1}MgAl$-P	0.3063	2.3356	10.3
$PtCuCe_{0.3}MgAl$-P	0.3065	2.3355	11.2
$PtCuCe_{0.6}MgAl$-P	0.3068	2.3390	10.6
$PtCuCe_{1.8}MgAl$-P	0.3065	2.3278	10.0
$PtCuCe_{3.0}MgAl$-P	0.3065	2.3303	10.6

[a] $a = 2d_{110}$

[b] $c = 3d_{003}$

[c] Crystallite size in *c*-direction is calculated by the Scherrer equation based on the half-height width of the (003) and (006) diffraction peaks of HTs

Compared with MgAl-P sample, the increase of *c* value for PtMgAl-P is related to the low charge density of the layer. The increase of *c* as well as the presence of only well crystallized HT phase mean that Pt^{4+} ions can be inserted into a layer of the HT structure. Indeed, the Pt^{4+} ions are most likely to form octahedrally coordinated compounds, unlike Pt^{2+} ions [32]. Furthermore, the enhanced *c* value implies that the Al^{3+} ions may not be fully co-precipitated in the HT phase when Pt^{4+} is in the mother liquid, which is proved by the ICP-OES results in Table 2. The slightly increased lattice parameter *a* of PtMgAl-P is related to the bigger radius of Pt^{4+} ions (0.063 nm) [30] in the octahedral coordination than that of Al^{3+} ions (0.054 nm), but the introduced amount of Pt^{4+} ions is so small that the effect on *a* is weak.

Certainly, we cannot exclude the presence of the partial metal ions in the amorphous phase on the basis of XRD result.

Table 2 Chemical compositions of the calcined samples

Sample	Pt/Cu/Ce/Mg/Al initial atomic ratio	Atomic ratio measured by ICP-OES	$(M^{4+}+M^{2+})/M^{3+}$ atomic ratio to initial one	Metal composition (wt%)[a]		
				Pt	Cu	Ce
PtMgAl-O	0.0056/0/0/3/1	0.0078/0/0/3.97/1	1.32	0.58	0	0
PtCuMgAl-O	0.0056/0.26/0/3/1	0.0076/0.37/0/4.19/1	1.40	0.47	7.5	0
$PtCuCe_{0.1}MgAl$-O	0.0056/0.26/0.0018/3/1	0.0077/0.37/0.0026/4.11/1	1.37	0.53	8.3	0.1 (0.1)
$PtCuCe_{0.3}MgAl$-O	0.0056/0.26/0.0046/3/1	0.0076/0.38/0.0060/4.09/1	1.37	0.52	8.3	0.3 (0.3)
$PtCuCe_{0.6}MgAl$-O	0.0056/0.26/0.0083/3/1	0.0075/0.37/0.0093/4.18/1	1.39	0.48	7.9	0.4 (0.6)
imp-PtCuMgAl-O	0.0056/0.26/0/3/1	0.011/0.42/0/4.73/1	1.58	0.62	7.6	0

[a]The numbers in parentheses are the nominal compositions in the synthesis mixture and those without parentheses are determined by ICP-OES analysis

Structure, Composition, and Texture of the Calcined Samples

The element analysis results provided in Table 2 show that the Pt/Cu/Ce/Mg/Al atomic ratios in the samples are different from those employed in the synthesis mixture; especially, the $(M^{4+}+M^{2+})/M^{3+}$ atomic ratio has a significant increase compared with the corresponding feeding amount, indicating an incomplete precipitation of the Al^{3+} ions. For the one-pot synthesized samples, the result reflects that the big Pt^{4+} ions (0.063 nm) are incorporated by partial substitution of the small Al^{3+} ions (0.054 nm) in octahedral coordination, and the loss of the Al^{3+} ions in imp-PtCuMgAl-O is mainly ascribed to the acidic leak of Al^{3+} ions from Mg(Al)O support during the impregnation. Furthermore, it can be found that the incorporation of Cu inhibits the insertion of Pt^{4+} ions in the layer. The Jahn–Teller distortion of the coordination environment around the Cu^{2+} ions can explain the difference. Subsequently, the addition of small amounts of Ce^{3+} ions can weaken the Jahn–Teller effect and enhance the capacity of Pt^{4+} and Cu^{2+} ions in the layer. The high Pt loading amount for imp-PtCuMgAl-O is mainly due to the weak physisorption during incipient wetness impregnation, which is independent of the formation of chemical bonds with other metal ions.

Figure 2 shows the XRD patterns of the calcined samples. The absence of the characteristic diffraction peaks of HT phase indicates that the layered structure has been destroyed. Instead, strong and sharp diffraction peaks of MgO (JCPDS file No. 04-0829) at 2θ of around 35.6°, 43.4°, and 62.7° are displayed in all samples [9]. Meanwhile, these diffraction peaks slightly shift toward larger angles compared with those of pure MgO crystallite phases ($2\theta = 42.9°$ and 62.3°). This is as a result of the incorporation of Al^{3+} into the MgO structure to form Mg(Al)O solid solution [33–35]. No obvious peaks associated with PtO_x can be detected for all Pt-containing samples, which can be attributed to the low content, small particle size, or a partial dissolution in the cubic

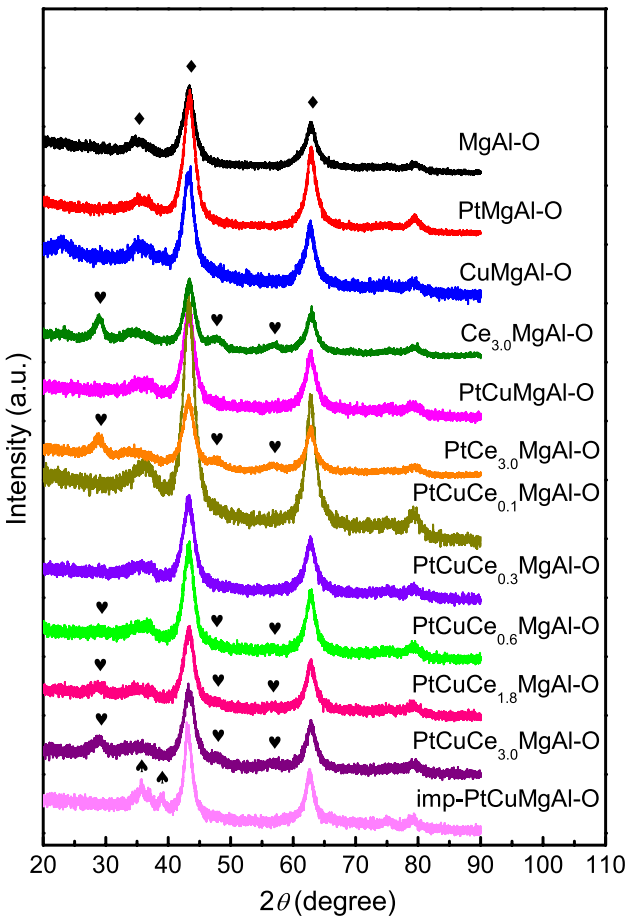

Fig. 2 XRD patterns of the calcined samples. (black diamond) Mg(Al)O periclase; (black heart) CeO_2; (black Spade) CuO

mixed oxides of Pt species [9]. For those Cu-containing samples, except the imp-PtCuMgAl-O, the diffraction peaks of CuO phase cannot be found, indicating that Cu^{2+} might have been incorporated into the MgO structure with Al^{3+} to form Mg(Cu, Al)O solid solution, such as Mg(Ni, Al)O, Mg(Co, Al)O, and Mg(Ni, Fe, Al)O, by the calcination

of the corresponding HTs [36–38]. This is associated with the well-distributed Cu^{2+} in the brucite-like layers. On the contrary, the sample imp-PtCuMgAl-O has visible diffraction peaks of CuO at 2θ of 35.6° and 38.9°, indicating the formation of a large CuO crystallite.

For the Ce-containing samples, the CeO_2 phase could not be detected until the Ce content was increased to above 0.3 wt%. The samples with Ce content greater than or equal to 0.6 wt% display clear peaks at 2θ of around 28.8°, 47.9°, and 56.8°, which can be attributed to the (111), (220), and (311) diffractions of CeO_2 (JCPDS file No. 43-1002) [21, 39]. It can be speculated that the CeO_2 phase also exists in the samples with low Ce content, although there are no visible diffraction peaks of CeO_2, which is due to the low content or small particle size of CeO_2 owing to its interaction with Pt and Cu species.

The textural properties of the samples are summarized in Table 3. The one-pot synthesized samples show higher BET specific surface areas, pore volumes, and pore sizes than the imp-PtCuMgAl-O sample prepared by impregnation method. It can be deduced that the metal particle size of the former samples is smaller than that of the latter, which has large CuO nanoparticles (NPs).

Structure of the Reduced Samples

The XRD patterns of the reduced catalysts are shown in Fig. 3. Here, Pt diffraction peaks were still not detected. Compared with the XRD patterns in Fig. 2, there are no changes in the diffraction peaks of Mg(Al)O periclase and CeO_2 phase over the reduced samples. This demonstrates that the reduction of these oxides is extremely limited [21]. For PtCu/MgAl-R, PtCu/Ce$_x$MgAl-R (x = 0.1, 0.3, and 0.6, respectively), the weak and broad diffraction peak at 2θ of 50.2° can be indexed to (200) reflection of cubic Cu (JCPDS file No. 04-0836), indicating that the Cu NPs have small particle sizes and are highly dispersed [40]. However, no obvious Cu diffraction peaks are detected for the samples with Ce content of 1.8 and 3.0 wt%, which can be ascribed to a high content of CeO_2 that promotes Cu dispersion. In addition, the imp-PtCu/MgAl-R presents strong and sharp Cu diffractions at 2θ of 43.3°, 50.4°, and 74.1°, which indicates a large crystal size formation and strong Cu crystallization.

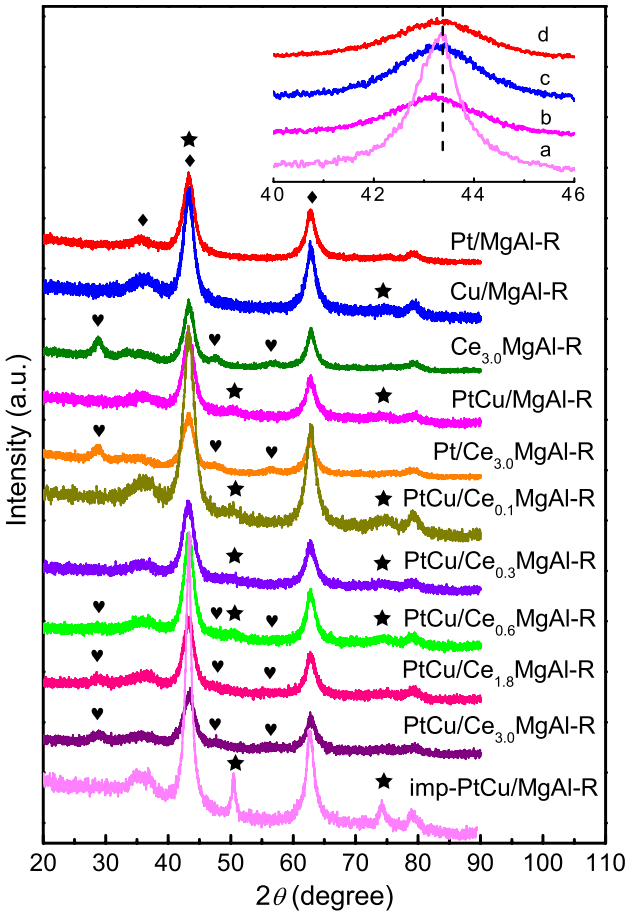

Fig. 3 XRD patterns of the reduced samples. (black diamond) Mg(Al)O periclase; (black heart) CeO_2; (black star) Cu. (inset: a. imp-PtCu/MgAl-R; b. PtCu/MgAl-R; c. Cu/MgAl-R; d. Pt/MgAl-R)

Table 3 Textural data of calcined samples

Sample	BET specific surface area (m^2 g^{-1})	Pore volume (cm^3 g^{-1})[a]	Average pore size (nm)[b]
PtMgAl-O	163	1.1	21.0
PtCe$_{3.0}$MgAl-O	170	1.1	25.0
PtCuMgAl-O	173	1.0	17.9
PtCuCe$_{0.1}$MgAl-O	204	1.2	18.1
PtCuCe$_{0.3}$MgAl-O	176	0.9	17.4
PtCuCe$_{0.6}$MgAl-O	175	1.2	21.8
PtCuCe$_{1.8}$MgAl-O	177	1.0	17.8
PtCuCe$_{3.0}$MgAl-O	185	1.1	19.5
imp-PtCuMgAl-O	130	0.6	12.5

[a]Analyzed at a P/P_0 value of 0.99

[b]Calculated using the BJH method

From the inset of Fig. 3, the peak at 2θ of 43.1° for PtCu/MgAl-R shifts slightly to the lower 2θ value compared with the position at 43.3° of the Cu diffraction for the Cu/MgAl-R sample. This indicates that Pt and Cu interacts on the formation of Pt–Cu alloy. Meanwhile, for the imp-PtCu/MgAl-R sample, the peak at 43.3° is unsymmetrical and broadens at the lower 2θ value, indicating the co-presence of Cu and Pt–Cu alloy [41–43].

The morphologies and particle size distributions (PSDs) of the metal species of the reduced samples are shown in Fig. 4. According to the lattice spacing of 0.226 nm in the HR-TEM image of Pt/MgAl-R, the Pt (111) plane can be

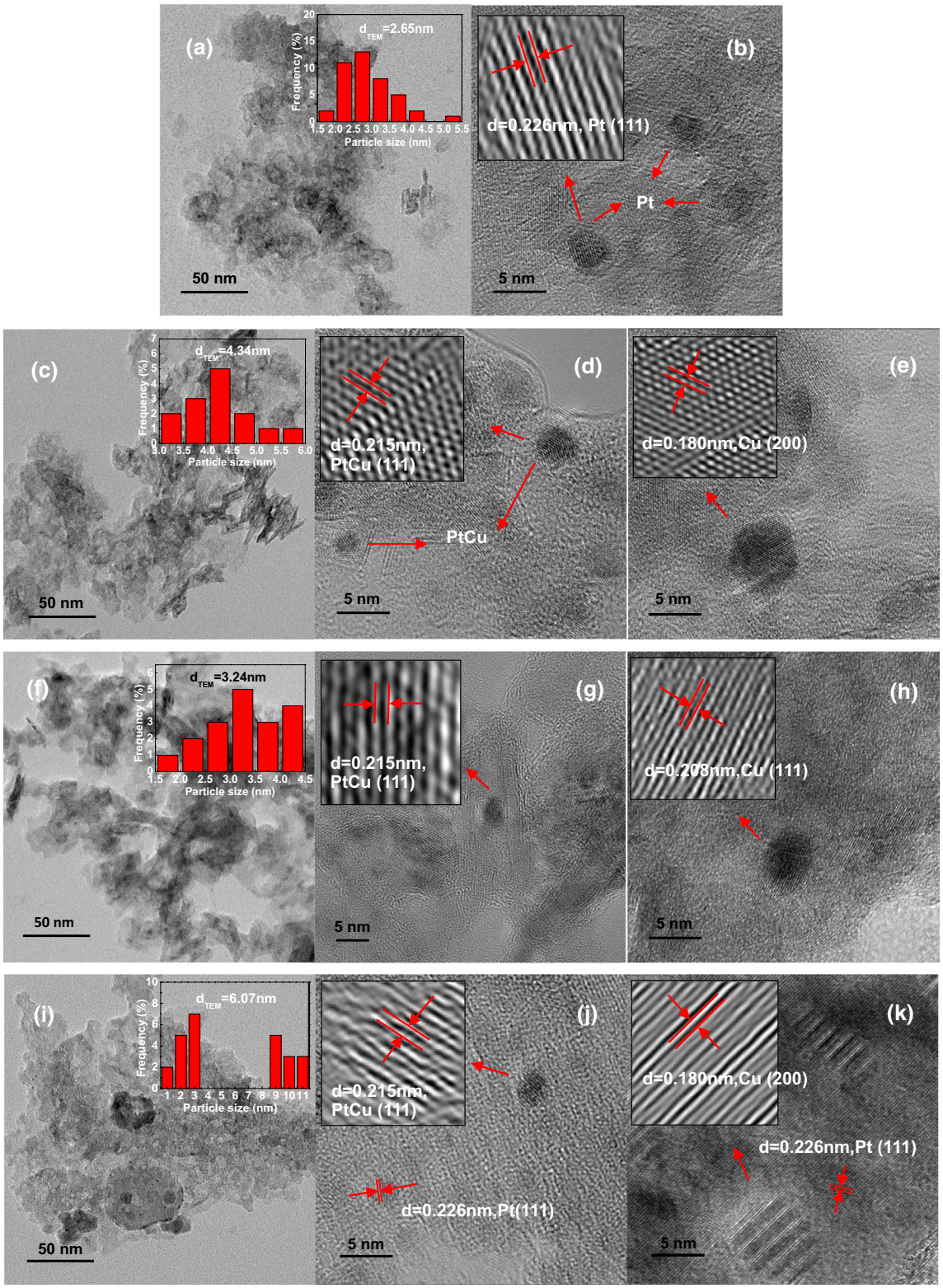

Fig. 4 HR-TEM images and particle size distribution of metal species for the catalysts of **a**, **b** Pt/MgAl-R; **c**, **d**, **e** PtCu/MgAl-R; **f**, **g**, **h** PtCu/$Ce_{0.3}$MgAl-R; **i**, **j**, **k** imp-PtCu/MgAl-R

confirmed. From the HR-TEM images (Fig. 4d, g, and j) of the other three catalysts, a lattice spacing of 0.215 nm of the metal NPs can be assigned to the (111) plane of the Pt–Cu alloy phase [10]. There is no obvious change in the particle size of the Pt–Cu alloy in all samples. In addition, small size Cu NPs exists in the samples PtCu/MgAl-R and PtCu/$Ce_{0.3}$MgAl-R. However, in the imp-PtCu/MgAl-R sample, isolated Pt NPs (Fig. 4j) and large Cu NPs (Fig. 4k) can be found, which can be ascribed to the inhomogeneous distribution of metal species.

The PSDs reflect a well-dispersed small metal NPs feature for the samples synthesized from HT precursor by one-pot method. The introduction of Cu results in a slight increase of average particle size from 2.65 nm of Pt/MgAl-R to 4.34 nm of PtCu/MgAl-R, and the average particle size further declines to 3.24 nm of PtCu/$Ce_{0.3}$MgAl-R following the incorporation of Ce. The slightly increased size of PtCu/MgAl-R metal NPs is related to the co-existence of Pt–Cu alloy and isolated Cu NPs. For PtCu/$Ce_{0.3}$MgAl-R, the reduced size indicates that the Ce-doping facilitates the dispersion of the Pt–Cu alloy and Cu NPs. However, the PSD of imp-PtCu/MgAl-R was split into two areas and the average particle size increased to 6.07 nm, mainly because of the large metal NPs formed by the aggregation of Cu NPs. The HT lattice-confined Pt^{4+}, Cu^{2+}, and Ce^{3+} ions are beneficial to playing the Ce-dispersing role and forming the interactions among metal NPs, involving the Pt–Cu alloy. On the contrary, the isolated Pt and Cu NPs not confined on the reduced catalysts surface are unstable and tend to aggregate into big particles. Thus, both the preparation method of catalysts and addition of Ce significantly affect the crystal properties of the reduced catalysts.

To identify the elemental distribution of the representative PtCu/$Ce_{0.3}$MgAl-R catalyst, the TEM-EDS mapping and line scan results are shown in Fig. 5. The results reveal a uniform distribution of Pt, Cu, and Ce on the support surface. This is due to the topotactic transformation feature of HT materials, which keeps the uniform mixing of every metal into the corresponding calcined samples and even reduced products [40].

In the line scan profile of PtCu/$Ce_{0.3}$MgAl-R, the peaks of Pt and Cu appear at the same position, indicating an intimate interaction between Pt and Cu, which clearly demonstrates that the well-dispersed Pt and Cu facilitated the Pt–Cu alloy formation in accordance with the above analyses. The Ce also has the same variation trend as Pt and Cu, suggesting that Ce has a close contact with Cu and Pt, which aids the dispersion and stabilization of Cu and Pt–Cu NPs.

From the CO chemisorption data in Table 4, it can be found that although CO can be adsorbed on both Pt and Cu surfaces, the CO uptake capacity can still reflect the overall metal dispersion of the catalysts. It can be concluded that the Pt/MgAl-R and imp-PtCu/MgAl-R samples have a low metal dispersion, while the Pt–Cu/$Ce_{0.3}$MgAl-R sample has

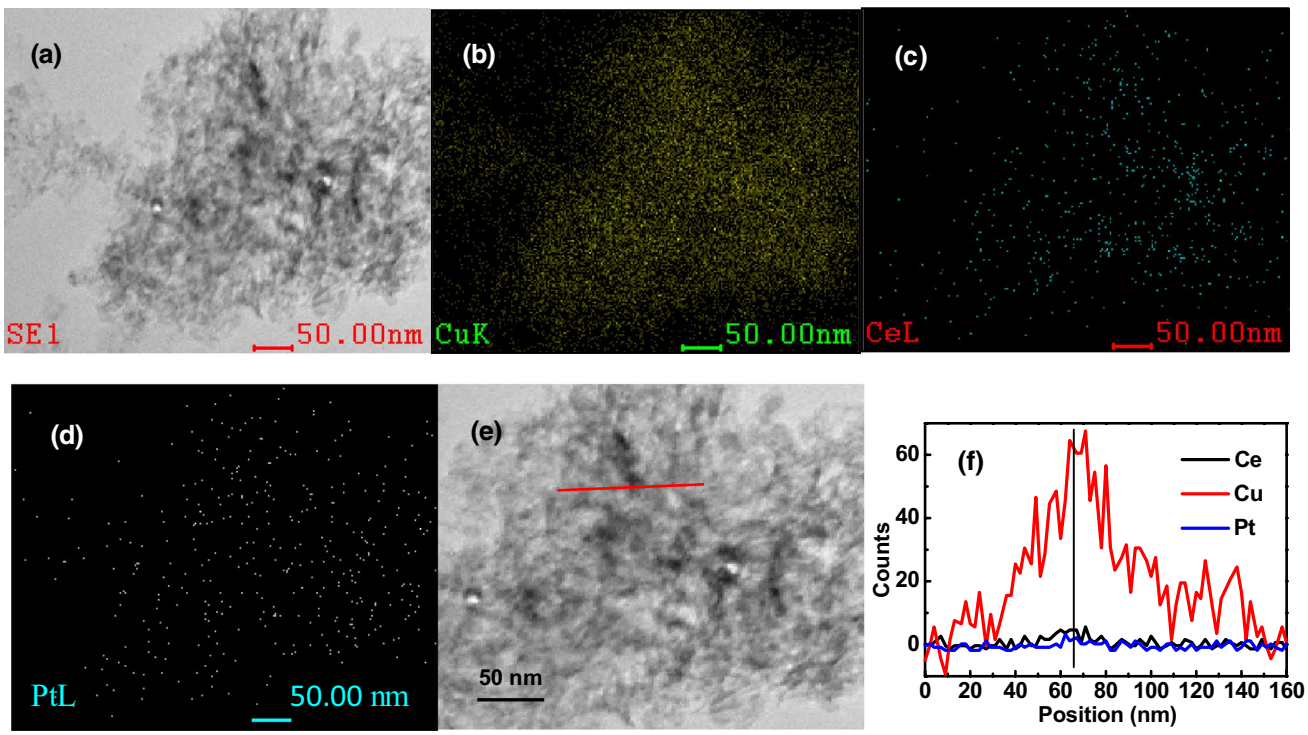

Fig. 5 TEM images with EDS element-mapping analysis (**a**–**d**) and line scan profile (**e** and **f**) of PtCu/$Ce_{0.3}$MgAl-R

Table 4 CO uptake on reduced samples

Sample	CO uptake ($\mu mol\ g_{cat}^{-1}$)[a]
Pt/MgAl-R	7.4
PtCu/MgAl-R	70.1
$PtCu/Ce_{0.3}MgAl$-R	86.2
imp-PtCu/MgAl-R	12.6

[a]Determined by CO chemisorption

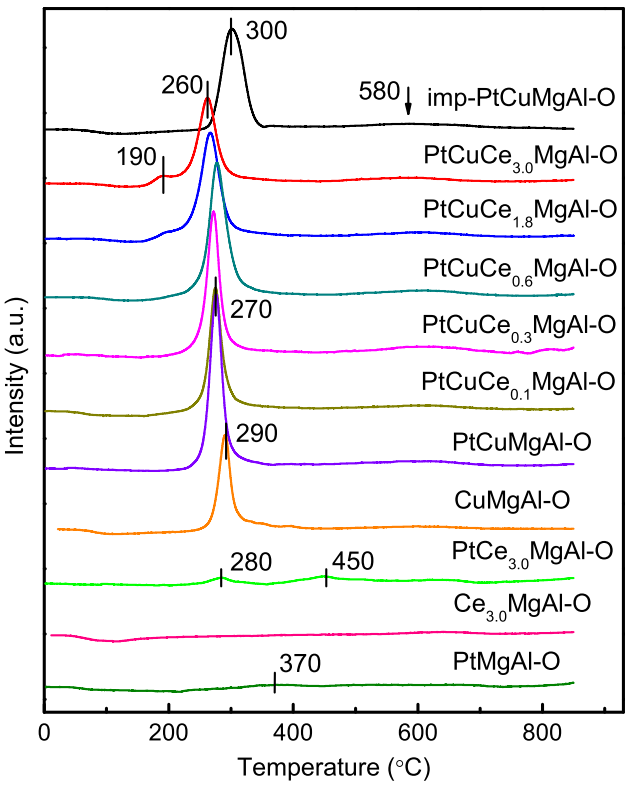

Fig. 6 H_2-TPR curves for the calcined samples

the highest metal dispersion because Ce can further promote Pt and Cu dispersion.

Reducible Properties

To examine the reducible properties of the calcined samples, H_2-TPR characterization was performed and the curves are shown in Fig. 6. For $Ce_{3.0}MgAl$-O, no obvious H_2 consumption can be observed. A faint bulge can be seen in PtMgAl-O, which is because of the reduction of PtO_x species. For the $PtCe_{3.0}MgAl$-O sample, there are two reduction peaks at 280 and 450 °C, whereby the lower temperature peak can be assigned to the reduction of Pt^{4+} ions and the higher temperature peak can be attributed to the partial reduction of CeO_2 [44]. This indicates that CeO_2 NPs disperse the Pt NPs and both of them can promote a mutual reduction [45]. In addition, from the XRD pattern (Fig. 3), the CeO_2-containing samples show clear CeO_2 diffraction peaks after reduction, which is highly consistent with the TPR results, indicating that the reduction of Ce oxide is extremely limited.

For the Cu-containing samples derived from HT precursors, a prominent hydrogen consumption peak is centered at around 150–350 °C, which is easily attributed to the reduction of surface Cu^{2+} to Cu^0 or the co-reduction of Pt and Cu, and the small and broad high-temperature shoulder at about 580 °C may be because of Cu^{2+} reduction in bulk. In the absence of noble metal, a strong peak at 290 °C can be observed for the CuMgAl-O catalyst. On the addition of noble metal Pt, this reduction peak shifts toward a lower temperature for the PtCuMgAl-O catalyst. The decreased reduction temperature of Cu^{2+} ions and the missing reduction peak of Pt^{4+} ions suggest that a strong interaction exists between Pt and Cu, which is the key to the formation of Pt–Cu alloy [46]. This result is consistent with the XRD and TEM analyses of the reduced samples [47]. However, the reduction behavior of the imp-PtCuMgAl-O shows a relatively higher temperature and broader reduction peak at 300 °C because of the PtO_x and large CuO NPs reduction.

In comparison with the PtCuMgAl-O catalyst, a small amount of Ce-doping ($PtCuCe_{0.3}MgAl$-O) can decrease the reduction peak temperature, indicating that the reducing ability is enhanced with the introduction of Ce species. At 1.8 wt% Ce content, a small frontal peak appears. The frontal peak and main peak temperatures decrease with further increase in Ce content. In addition, the frontal peak area shows an increasing tendency accompanied by the decrease of the main peak area. It can be deduced that the frontal peak belongs to the reduction of Pt^{4+} ions and the main peak should be related to the co-reduction of Pt and Cu species. This indicates that the Pt and Cu interaction becomes weak because of the dilution effect of excessive Ce. Thus, the Ce species significantly affects the dispersion of other metal species. Its content needs to be controlled to ensure a moderate dispersion and a consequent interaction for other metal species.

X-ray photoelectron spectroscopy (XPS) characterization has been carried out to investigate the chemical state of Cu element in the prepared catalysts. The Cu $2p_{3/2}$ XPS spectra are shown in Fig. 7 and the corresponding results of the surface Cu state are listed in Table 5. The XPS spectra of Pt 4*f* in all samples are not given because of the difficulty in distinguishing Pt 4*f* peak from Cu 3*p* and Al 2*p* peaks caused by their overlapping [46, 48] and the extremely small Pt loading (0.47–0.62 wt%) [4].

In Fig. 7, the obvious satellite peaks located at 939.0–947.0 eV indicate the presence of Cu^{2+} ions. The source of the satellite peaks is either the promotion of 3*d* electrons to 4*p* and/or 4*s* levels or the charge transfer of

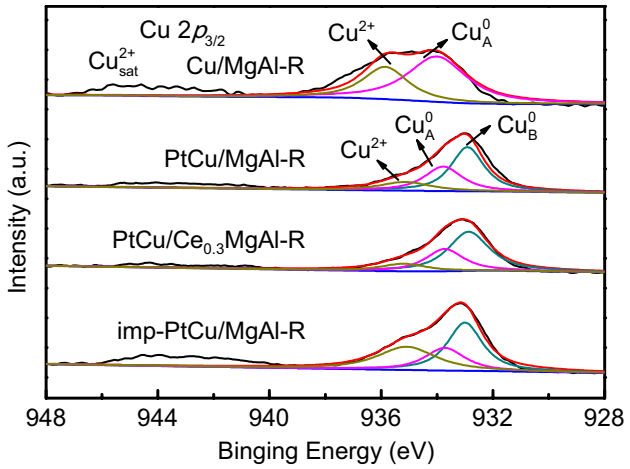

Fig. 7 XPS spectra of the Cu $2p_{3/2}$ in the representative samples: Cu/MgAl-R, PtCu/MgAl-R, PtCu/$Ce_{0.3}$MgAl-R, and imp-PtCu/MgAl-R

electrons to the unfilled 3*d*, so that the transfer cannot occur in Cu^+ and Cu^0 because of their completely filled 3*d* shells [46]. For Cu/MgAl-R, the Cu $2p_{3/2}$ peak can be fitted into two peaks at 934.0 and 935.8 eV, corresponding to the Cu^0 and Cu^{2+} ions, respectively. Compared with the Cu/MgAl-R, the Cu 2*p* level of other samples shifts to the lower binding energy, which is caused by Pt–Cu alloy, and this phenomenon occurred in previous studies. Cho [49] and Kleiman [50] systematically studied the charge transfer in Pt–Cu alloy and revealed that the Cu 2*p* level exhibited a negative shift upon alloying with Pt. For the PtCu/MgAl-R sample, the peak is deconvoluted into three contributions centered at about 935.1, 933.7, and 932.9 eV. The minor contribution at 935.1 eV is because of the unreduced Cu^{2+} ions in the bulk which strongly interact with the support and are difficult to be reduced, while the peaks at 933.7 and 932.9 eV are ascribed to the isolated metallic Cu (Cu^0_A) and Cu^0 in Pt–Cu alloy (Cu^0_B), respectively. The absence of Cu^+ species in the spectra indicates that Cu^{2+} ions were directly reduced to Cu^0. A similar situation was encountered in the PtCu/$Ce_{0.3}$MgAl-R and imp-PtCu/MgAl-R.

A slightly increased binding energy value for Cu^{2+} ions can be observed in Table 5, which is in accordance with the order of imp-PtCu/MgAl-R, PtCu/MgAl-R, PtCu/$Ce_{0.3}$MgAl-R, and Cu/MgAl-R. This is related to an increased surface interaction between Cu^{2+} ions and other near groups. It signifies that the Cu^{2+} ions in imp-PtCu/MgAl-R are unstable. Furthermore, according to the proportion of the Cu^{2+} ions, it is clear that the impregnation method favors Cu^{2+} species more than Cu^0 species, which can be due to the difficult reduction of large CuO NPs in imp-PtCu/MgAl-R. It can be predicted that a large amount of unstable Cu^{2+} ions tends to shorten the operational lifespan of imp-PtCu/MgAl-R. On the contrary, the binging energy of Cu^0_B decreases across imp-PtCu/MgAl-R, PtCu/MgAl-R, and PtCu/$Ce_{0.3}$MgAl-R. This indicates that the interaction strength between Pt and Cu decreased slightly. However, it is suggested that the chemical activity of Pt and Cu species in these catalysts increases in the same order. In addition, the sequence of the Cu^0_B proportion is as follows: imp-PtCu/MgAl-R < PtCu/MgAl-R < PtCu/$Ce_{0.3}$MgAl-R, indicating an increase of the Pt–Cu alloy sites. However, there is no difference for the binding energy value of the isolated Cu^0_A species, which reflects that the interaction between the adjacent metal elements and Cu^0_A species is the same among the samples. However, the Cu^0_A proportion increases across imp-PtCu/MgAl-R, PtCu/$Ce_{0.3}$MgAl-R, and PtCu/MgAl-R. Based on the same preparation method, the lesser the amount of Cu^0_A, the stronger the stability of the catalysts.

Catalytic Performance

To compare results, the PDH of the reduced catalysts is tested. Figure 8 presents the propane conversion, propene selectivity and yield over the reduced catalysts. The propane conversions of Pt/MgAl-R and Cu/MgAl-R catalysts are below 10%, and the propene selectivities and yields are below 75% and below 10%, respectively. Although the initial conversion of Pt/$Ce_{3.0}$MgAl-R is close to 100%, the initial propene selectivity and yield are nearly zero; this indicates that the Ce element has a good dispersion effect on the Pt NPs, which results in a high Pt NPs activity and deep dehydrogenation and cracking [7, 51]. It can be deduced that the Pt NPs can be dispersed into Pt single atoms by Ce, which accounts for the 100% propane conversion over Pt/

Table 5 XPS characteristics of Cu $2p_{3/2}$ region for the catalysts

Sample	Cu $2p_{3/2}$ binding energy (eV)			Peak intensity (%)		
	Cu^0_B	Cu^0_A	Cu^{2+}	I (Cu^0_B)[b]	I (Cu^0_A)	I (Cu^{2+})
Cu/MgAl-R		934.0 (2.5)	935.8 (1.9)		66.8	33.1
PtCu/MgAl-R	932.9 (1.4)[a]	933.7 (1.6)	935.1 (2.1)	51.5	32.7	15.7
PtCu/$Ce_{0.3}$MgAl-R	932.8 (1.7)	933.7 (1.6)	935.2 (1.9)	57.2	30.2	12.4
imp-PtCu/MgAl-R	933.0 (1.4)	933.7 (1.7)	935.0 (2.4)	42.5	22.9	34.4

[a]Numbers in parentheses are the FWHM of the fitted peaks in eV

[b]Intensity of the peaks as a percentage of the total Cu $2p_{3/2}$ area

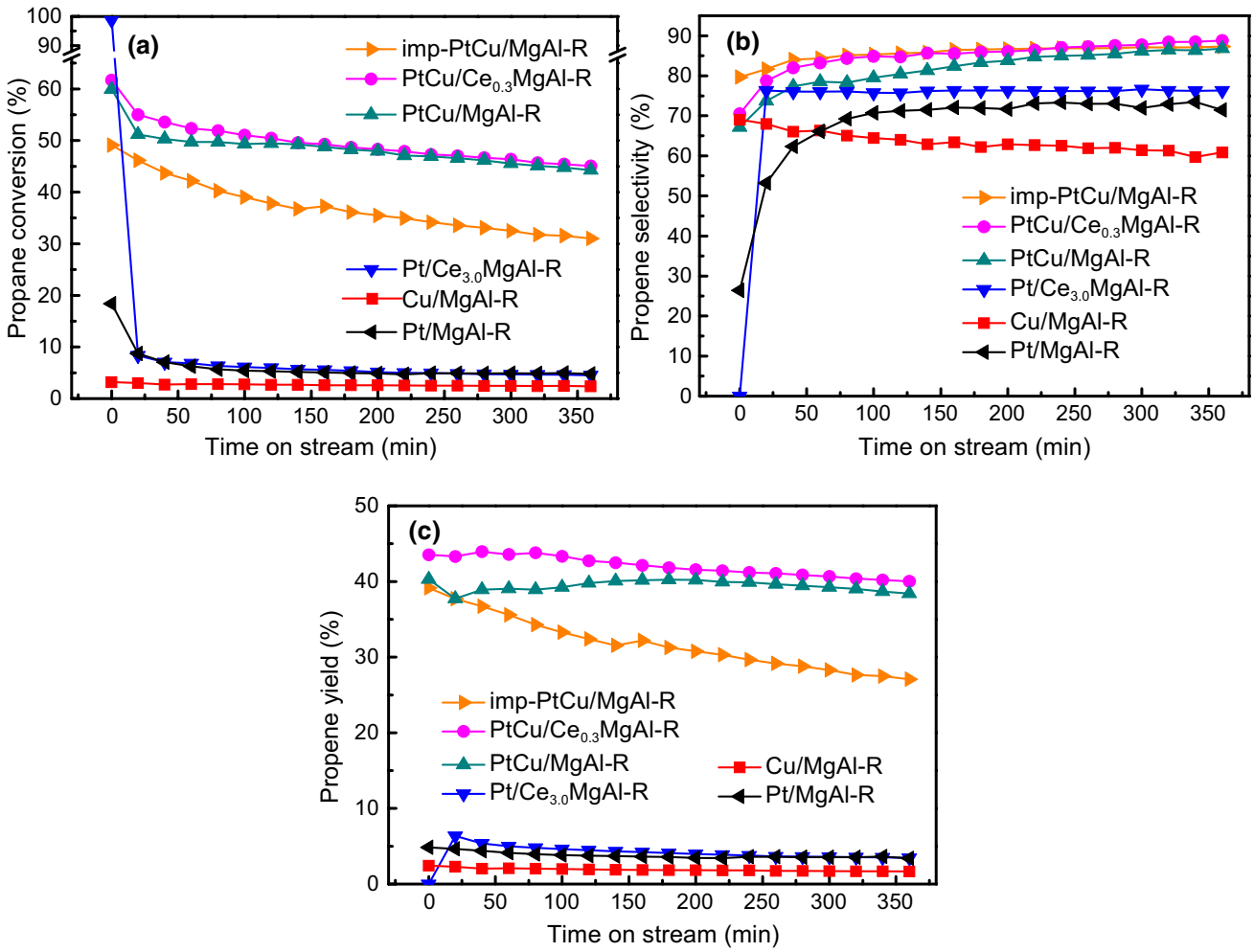

Fig. 8 Propane conversion, propene selectivity and yield over reduced catalysts. Reaction conditions: 600 °C, atmospheric pressure, C_3H_8:H_2:N_2 (molar ratio) = 8:7:35, and WHSV = 3 h^{-1}

$Ce_{3.0}$MgAl-R at the initial stage. However, the unstable Pt atoms on Pt/$Ce_{3.0}$MgAl-R can be rapidly aggregated into large Pt NPs and decrease catalytic performance.

The co-introduction of Pt and Cu significantly enhanced the PDH performance, as the interaction between Pt and Cu accounted for the high catalytic activity of PDH [10]. The initial propane conversion of PtCu/MgAl-R is higher than that of imp-PtCu/MgAl-R and slightly lower than that of PtCu/$Ce_{0.3}$MgAl-R. After spending 360 min in the gas stream, the conversion of PtCu/MgAl-R, PtCu/$Ce_{0.3}$MgAl-R and imp-PtCu/MgAl-R decreased from 60, 62, and 49 to 44, 45, and 31%, respectively. The slightly higher activity of PtCu/$Ce_{0.3}$MgAl-R than that of PtCu/MgAl-R can be attributed to the high dispersion of Pt–Cu alloy and Cu NPs promoted by Ce, which is supported by the results of CO chemisorption in Table 4. The corresponding low activity of imp-PtCu/MgAl-R is related to the poor Cu dispersion and lack of interaction between Pt and Cu. The basic reason is the different structural features between the PtCu/$Ce_{0.3}$MgAl-R and PtCu/MgAl-R obtained by one-pot synthesis from HT precursor and imp-PtCu/MgAl-R prepared by impregnation.

From Fig. 8b, the interaction between Pt and Cu favors the selectivity to propene by inhibiting propene adsorption and improving the energy barrier of C–C bond breakage [10]. During the 360 min reaction time, the PtCu/$Ce_{0.3}$MgAl-R propene selectivity is similar to that of imp-PtCu/MgAl-R and slightly higher than that of PtCu/MgAl-R. Even their propene selectivity plots cannot be distinguished after the 360 min reaction. According to the structural features of these catalysts, the similar selectivity is only correlated with the presence of Pt–Cu alloy, but independent of the content and interaction strength of Pt–Cu alloy.

The propene yield increases in the following order: imp-PtCu/MgAl-R < PtCu/MgAl-R < PtCu/$Ce_{0.3}$MgAl-R, indicating that the catalytic performance follows the same increasing trend. During the reaction, the PtCu/$Ce_{0.3}$MgAl-R catalyst affords the highest propene yield of around 43.5%

(around 40.2% for PtCu/MgAl-R and around 39.1% for imp-PtCu/MgAl-R). The presence of a large number of highly dispersed Pt–Cu alloy sites enhances the productivity of PtCu/$Ce_{0.3}$MgAl-R to propene. However, a sharp decrease of propene yield is observed in imp-PtCu/MgAl-R, hinting that imp-PtCu/MgAl-R has a shorter lifespan than PtCu/$Ce_{0.3}$MgAl-R and PtCu/MgAl-R. This can be attributed to the less Pt–Cu alloy sites and poor dispersion of metal species on the imp-PtCu/MgAl-R surface, which results in the aggregation and sintering of isolated Pt and Cu NPs during the high-temperature reaction.

The effect of Ce content on the catalytic performance of PDH is illustrated in Fig. 9. Comparing PtCu/$Ce_{0.1}$MgAl-R and PtCu/$Ce_{0.6}$MgAl-R, the PtCu/$Ce_{0.3}$MgAl-R catalyst has a much better conversion and yield, but they both have a similar propene selectivity. This suggests that the Ce species on the surface of the catalysts noticeably influences the catalytic performance. The optimal Ce content was confirmed to be 0.3 wt%, which is related to the formation of a great amount of Pt–Cu alloy sites and high dispersion of active Pt–Cu centers and other metal species on the PtCu/$Ce_{0.3}$MgAl-R surface.

Deactivation Analysis

The TG spectra of the used catalysts are shown in Fig. 10. The calculated weight losses of the used Pt/MgAl-R, PtCu/MgAl-R, PtCu/$Ce_{0.3}$MgAl-R and imp-PtCu/MgAl-R are 17.1, 47.1, 35.9, and 13.9%, respectively. The weight loss is mainly due to the removal of deposited coke. Usually, the higher the dehydrogenation activity of the catalyst, the easier the coke formation. However, the amount of coke formation over PtCu/$Ce_{0.3}$MgAl-R is less than that of PtCu/MgAl-R. This suggests that the coke resistance can be enhanced by adding Ce, because the high oxygen

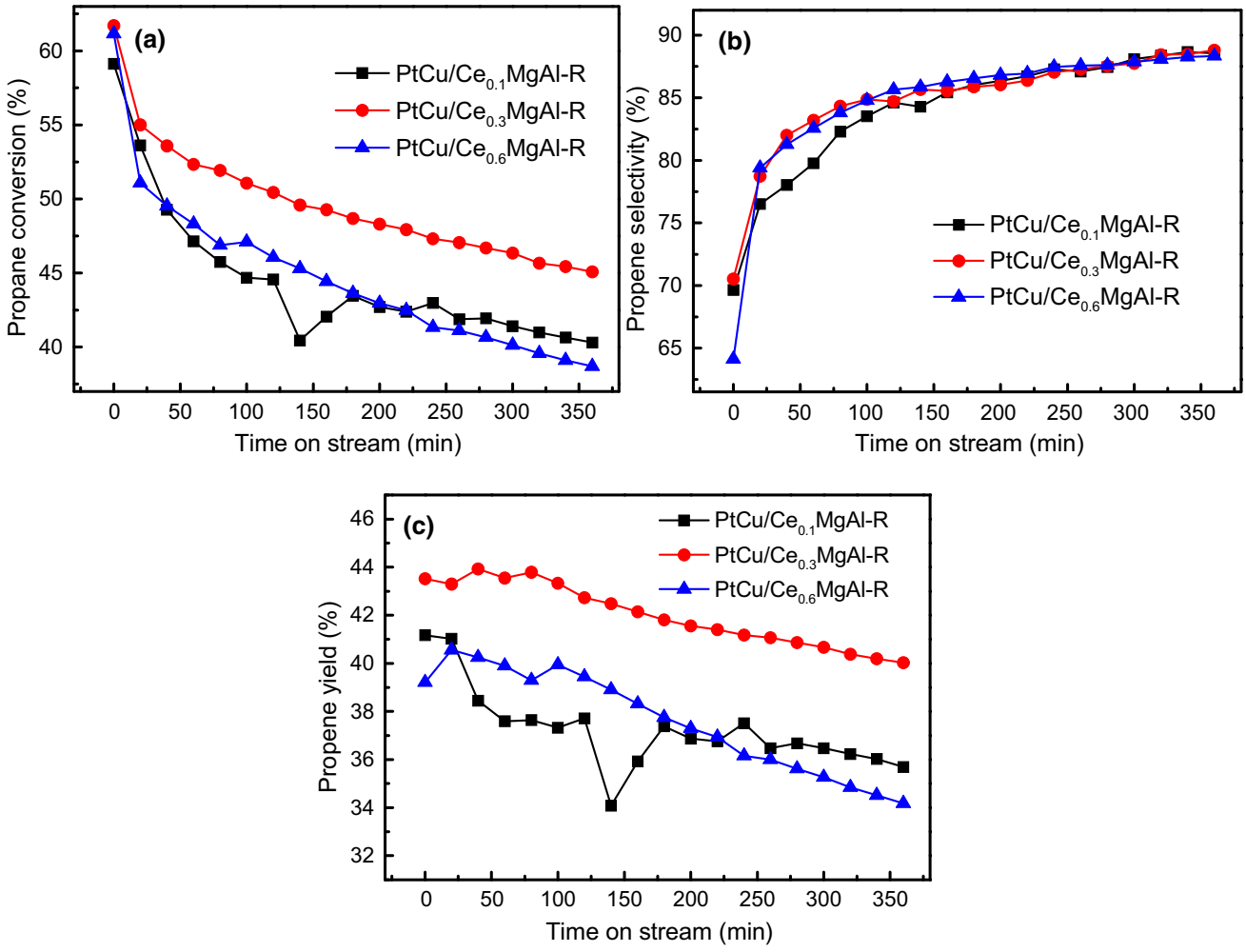

Fig. 9 Variation of **a** propane conversion, **b** propene selectivity, **c** propene yield for PDH with time over PtCu/Ce_xMgAl-R with different Ce contents. Reaction conditions: 600 °C, atmospheric pressure, C_3H_8:H_2:N_2 (molar ratio) = 8:7:35, and WHSV = 3 h^{-1}

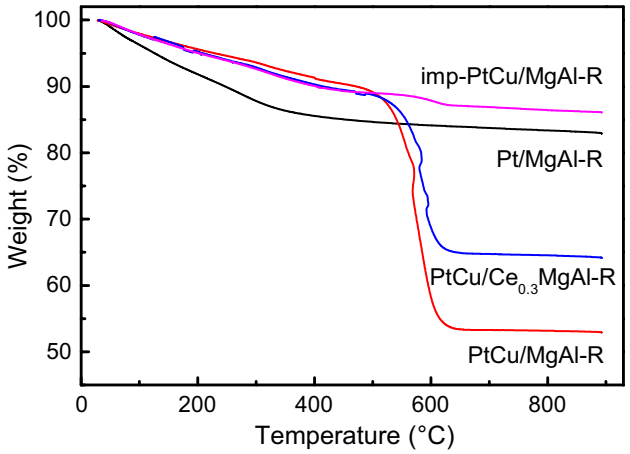

Fig. 10 TG profiles of the used catalysts

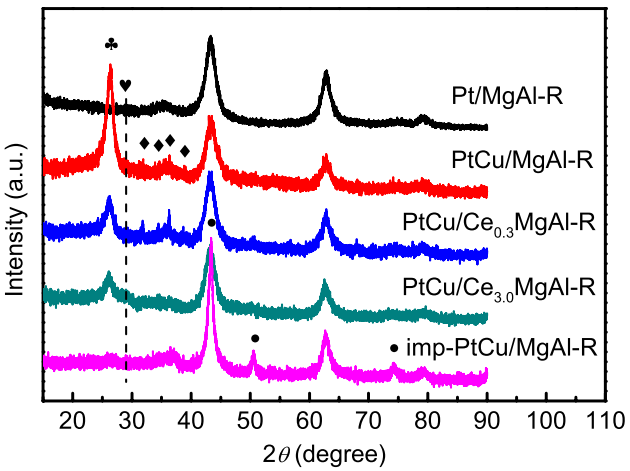

Fig. 11 XRD patterns of the used catalysts. (black diamond) Al_2O_3; (black heart) CeO_2; (black Club) graphitic carbon; (black circle) Cu

storage capacity of CeO_2 can promote the gasification of coke on the catalyst by storing and delivering active oxygen species.

The used catalysts were analyzed by XRD and the results are shown in Fig. 11. In comparison with the XRD patterns of the reduced catalysts in Fig. 3, the most remarkable change for the used catalyst is the appearance of a graphitic carbon diffraction at 2θ of about 26°, and the intensity of the peak decreases in the order of PtCu/MgAl-R > PtCu/$Ce_{0.3}$MgAl-R > PtCu/$Ce_{3.0}$MgAl-R > imp-PtCu/MgAl-R > Pt/MgAl-R. This order is similar to that of the total amount of carbon formation of these catalysts, indicating that the coke deposit is mainly graphitic carbon. Moreover, an Al_2O_3 phase appears for all samples, which may be because of the prolonged high-temperature reaction that leads to the phase separation of Al_2O_3 from Mg(Al)O solid solution.

The TEM images of the used catalysts are illustrated in Fig. 12, where the metal NPs are surrounded by carbon materials with thin graphene sheets [52]. In Fig. 12h and l, few carbon nanotubes can be found on the used PtCu/$Ce_{0.3}$MgAl-R and relatively big carbon nanotubes can be found on the used imp-PtCu/MgAl-R.

Moreover, a visible change in the dispersion and size of metal NPs in all samples can be observed among the catalysts before and after 360 min of PDH reaction. In fact, there is almost no aggregation of metal NPs on PtCu/$Ce_{0.3}$MgAl-R. This indicates an excellent anti-sintering ability for Pt–Cu alloy NPs in PtCu/$Ce_{0.3}$MgAl-R. For sample imp-PtCu/MgAl-R, large Cu NPs were observed accompanied by small Pt–Cu alloy NPs after PDH reaction at 600 °C for 360 min, indicating severe sintering of Cu NPs as well as superior anti-sintering of Pt–Cu alloy. The sintering degree is determined by the amount of the isolated metal ions. In other words, the highly dispersed Pt–Cu alloy NPs are more stable than isolated metal NPs, suggesting that the more the amount of Pt–Cu alloy NPs, the better the stability of the catalyst structures.

Conclusions

A series of CeO_2-modified PtCu/Mg(Al)O catalysts (PtCu/Ce_xMgAl-R) with different Ce contents were obtained by one-pot synthesis from HT-like precursors. Sites of Pt–Cu alloy were formed and were highly dispersed by CeO_2 NPs which interacted with Mg(Al)O support. The Pt–Cu alloy is the main active phase in PtCu/$Ce_{0.3}$MgAl-R, unlike the contrast sample with isolated large Cu phase; this leads to a high catalytic activity and propene yield in the PDH reaction. The introduction of Cu can effectively stabilize and disperse Pt NPs by forming Pt–Cu alloy, and the subsequent addition of 0.3 wt% Ce can further disperse Pt by increasing the Pt–Cu alloy sites and improve resistance to sintering and coke deposition. The excellent catalytic behavior of CeO_2-modified Pt–Cu alloy in PDH can enhance supported Pt–Cu bimetallic catalysts for a better performance in the dehydrogenation of light alkanes.

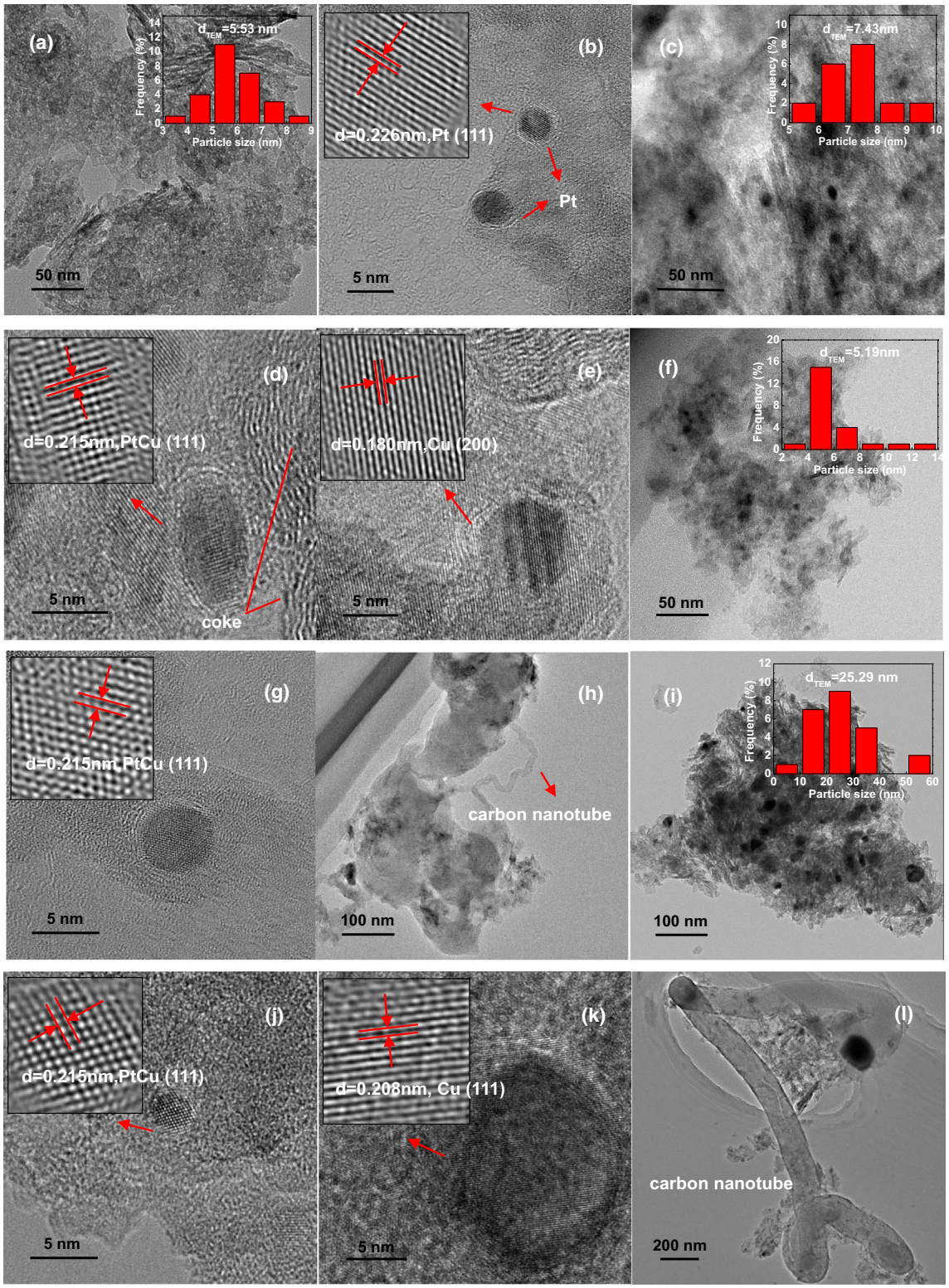

Fig. 12 TEM images and particle size distribution of metal particles over the used catalysts of **a**, **b** Pt/MgAl-R, **c**, **d**, **e** PtCu/MgAl-R, **f**, **g**, **h** PtCu/$Ce_{0.3}$MgAl-R, **i**, **j**, **k**, **l** imp-PtCu/MgAl-R

Acknowledgements This study was supported by the National Natural Science Foundation of China (No. 21776214), the Natural Science Foundation of Jiangsu Province (No. BK20161166), and the State Key Laboratory of Chemical Resource Engineering.

References

1. Baek J, Yun HJ, Yun D et al (2012) Preparation of highly dispersed chromium oxide catalysts supported on mesoporous silica for the oxidative dehydrogenation of propane using CO_2: insight into the nature of catalytically active chromium sites. ACS Catal 2(9):1893–1903
2. Sun PP, Siddiqi G, Chi M et al (2010) Synthesis and characterization of a new catalyst Pt/Mg(Ga)(Al)O for alkane dehydrogenation. J Catal 274(2):192–199
3. Long LL, Xia K, Lang WZ et al (2017) The comparison and optimization of zirconia, alumina, and zirconia-alumina supported PtSnIn trimetallic catalysts for propane dehydrogenation reaction. J Ind Eng Chem 51:271–280
4. Im J, Choi M (2016) Physicochemical stabilization of Pt against sintering for a dehydrogenation catalyst with high activity, selectivity, and durability. ACS Catal 6(5):2819–2826
5. Zhang YW, Zhou YM, Qiu AD et al (2006) Propane dehydrogenation on PtSn/ZSM-5 catalyst: effect of tin as a promoter. Catal Commun 7(11):860–866
6. Zhang YW, Zhou YM, Huang L et al (2011) Sn-modified ZSM-5 as support for platinum catalyst in propane dehydrogenation. Ind Eng Chem Res 50(13):7896–7902
7. Wang T, Jiang F, Liu G et al (2016) Effects of Ga doping on Pt/CeO_2–Al_2O_3 catalysts for propane dehydrogenation. AIChE J 62(12):4365–4376
8. Ma ZX, Wu ZW, Miller JT (2017) Effect of Cu content on the bimetallic Pt–Cu catalysts for propane dehydrogenation. Catal Struct React 3(1–2):43–53
9. Shen LL, Xia K, Lang WZ et al (2017) The effects of calcination temperature of support on PtIn/Mg(Al)O catalysts for propane dehydrogenation reaction. Chem Eng J 324:336–346
10. Han ZP, Li SR, Jiang F et al (2014) Propane dehydrogenation over Pt–Cu bimetallic catalysts: the nature of coke deposition and the role of copper. Nanoscale 6(17):10000–10008
11. Liu X, Lang WZ, Long LL et al (2014) Improved catalytic performance in propane dehydrogenation of $PtSn/\gamma$-Al_2O_3 catalysts by doping indium. Chem Eng J 247:183–192
12. Shi L, Deng GM, Li WC et al (2015) Al_2O_3 nanosheets rich in pentacoordinate Al^{3+} ions stabilize Pt–Sn clusters for propane dehydrogenation. Angew Chem Int Edit 54(47):13994–13998
13. Wegener EC, Wu Z, Tseng HT et al (2018) Structure and reactivity of Pt–In intermetallic alloy nanoparticles: highly selective catalysts for ethane dehydrogenation. Catal Today 299:146–153
14. Yu CL, Xu HY, Ge QJ et al (2007) Properties of the metallic phase of zinc-doped platinum catalysts for propane dehydrogenation. J Mol Catal A Chem 266(1–2):80–87
15. Xia K, Lang WZ, Li PP et al (2016) The influences of Mg/Al molar ratio on the properties of PtIn/Mg(Al)O-*x* catalysts for propane dehydrogenation reaction. Chem Eng J 284:1068–1079
16. Veldurthi S, Shin CH, Joo OS et al (2012) Promotional effects of Cu on Pt/Al_2O_3 and Pd/Al_2O_3 catalysts during n-butane dehydrogenation. Catal Today 185(1):88–93
17. de Lima SM, da Silva AM, da Costa LOO et al (2009) Study of catalyst deactivation and reaction mechanism of steam reforming, partial oxidation, and oxidative steam reforming of ethanol over Co/CeO_2 catalyst. J Catal 268(2):268–281
18. Lee Y, He G, Akey AJ et al (2011) Raman analysis of mode softening in nanoparticle $CeO_{2-\delta}$ and Au–$CeO_{2-\delta}$ during CO oxidation. J Am Chem Soc 133(33):12952–12955
19. Ilieva L, Pantaleo G, Ivanov I et al (2006) Gold catalysts supported on CeO_2 and CeO_2–Al_2O_3 for NO_x reduction by CO. Appl Catal B Environ 65(1–2):101–109
20. Mi JX, Gao YN, Zhang JC et al (2018) Effect of Ce modification on the structural and catalytic property of Co–Mo/Mg(Al)O catalyst for water-gas shift reaction. Appl Catal A Gen 553:36–42
21. Ren HP, Song YH, Wang W et al (2015) Insights into CeO_2-modified Ni–Mg–Al oxides for pressurized carbon dioxide reforming of methane. Chem Eng J 259:581–593
22. Zhang YW, Xue MW, Zhou YM et al (2016) Propane dehydrogenation over Ce-containing ZSM-5 supported platinum-tin catalysts: Ce concentration effect and reaction performance analysis. RSC Adv 6(35):29410–29422
23. Zhang YW, Zhou YM, Shi JJ et al (2014) Comparative study of bimetallic Pt–Sn catalysts supported on different supports for propane dehydrogenation. J Mol Catal A Chem 381:138–147
24. Llorca J, Homs N, León J et al (1999) Supported Pt–Sn catalysts highly selective for isobutane dehydrogenation: preparation, characterization and catalytic behavior. Appl Catal A Gen 189(1):77–86
25. Tang CM, Zhai ZJ, Li XL et al (2015) Highly efficient and robust $Mg_{0.388}Al_{2.408}O_4$ catalyst for gas-phase decarbonylation of lactic acid to acetaldehyde. J Catal 329:206–217
26. Akporiaye D, Jensen SF, Olsbye U et al (2001) A novel, highly efficient catalyst for propane dehydrogenation. Ind Eng Chem Res 40(22):4741–4748
27. Wu J, Peng ZM, Sun PP et al (2014) n-Butane dehydrogenation over Pt/Mg(In)(Al)O. Appl Catal A Gen 470:208–214
28. Redekop EA, Galvita VV, Poelman H et al (2014) Delivering a modifying element to metal nanoparticles via support: Pt–Ga alloying during the reduction of Pt/Mg(Al, Ga)Ox catalysts and its effects on propane dehydrogenation. ACS Catal 4(6):1812–1824
29. Nivangune NT, Ranade VV, Kelkar AA (2017) MgFeCe ternary layered double hydroxide as highly efficient and recyclable heterogeneous base catalyst for synthesis of dimethyl carbonate by transesterification. Catal Lett 147(10):2558–2569
30. Shannon RD (1976) Revised effective ionic radii and systematic studies of interatomic distances in halides and chalcogenides. Acta Crystall A 32:751–767
31. Zhang LH, Li F, Evans DG et al (2010) Cu–Zn–(Mn)–(Fe)–Al layered double hydroxides and their mixed metal oxides: physicochemical and catalytic properties in wet hydrogen peroxide oxidation of phenol. Ind Eng Chem Res 49:5959–5968
32. Basile F (2000) Synthesis and thermal evolution of hydrotalcite-type compounds containing noble metals. Appl Clay Sci 16:185–200
33. Yamaguchi K (1999) Mg–Al mixed oxides as highly active acid–base catalysts for cycloaddition of carbon dioxide to epoxides. J Am Chem Soc 121:4526–4527
34. Millange F, Walton RI, O'Hare D (2000) Time-resolved in situ X-ray diffraction study of the liquid-phase reconstruction of Mg–Al–carbonate hydrotalcite-like compounds. J Mater Chem 10:1713–1720
35. Prescott HA, Li ZJ, Kemnitz E et al (2005) Application of calcined Mg–Al hydrotalcites for Michael additions: an investigation of catalytic activity and acid–base properties. J Catal 234(1):119–130
36. Li D, Wang L, Koike M et al (2011) Steam reforming of tar from pyrolysis of biomass over Ni/Mg/Al catalysts prepared from hydrotalcite-like precursors. Appl Catal B Environ 102(3–4):528–538

37. Wang L, Li D, Watanabe H et al (2014) Catalytic performance and characterization of Co/Mg/Al catalysts prepared from hydrotalcite-like precursors for the steam gasification of biomass. Appl Catal B Environ 150–151:82–92
38. Li D, Koike M, Wang L et al (2014) Regenerability of hydrotalcite-derived nickel–iron alloy nanoparticles for syngas production from biomass tar. Chemsuschem 7(2):510–522
39. Jabłońska M, Nothdurft K, Nocuń M et al (2017) Redox-performance correlations in Ag–Cu–Mg–Al, Ce–Cu–Mg–Al, and Ga–Cu–Mg–Al hydrotalcite derived mixed metal oxides. Appl Catal B Environ 207:385–396
40. Li D, Cai YB, Chen CQ et al (2016) Magnesium–aluminum mixed metal oxide supported copper nanoparticles as catalysts for water–gas shift reaction. Fuel 184:382–389
41. Zhao XY, Luo BB, Long R et al (2015) Composition-dependent activity of Cu–Pt alloy nanocubes for electrocatalytic CO_2 reduction. J Mater Chem A 3(8):4134–4138
42. Liu JJ, Zou SH, Xiao LP et al (2014) Well-dispersed bimetallic nanoparticles confined in mesoporous metal oxides and their optimized catalytic activity for nitrobenzene hydrogenation. Catal Sci Technol 4(2):441–446
43. Qiao PS, Zou SH, Xu SD et al (2014) A general synthesis strategy of multi-metallic nanoparticles within mesoporous titania via in situ photo-deposition. J Mater Chem A 2(41):17321–17328
44. Kam R, Scott J, Amal R et al (2010) Pyrophoricity and stability of copper and platinum based water–gas shift catalysts during oxidative shut-down/start-up operation. Chem Eng Sci 65(24):6461–6470
45. Ozawa M, Takahashi-Morita M, Kobayashi K et al (2017) Core–shell type ceria zirconia support for platinum and rhodium three way catalysts. Catal Today 281:482–489
46. Barrabés N, Frare A, Föttinger K et al (2012) Pt–Cu bimetallic catalysts obtained from layered double hydroxides by an anion-exchange route. Appl Clay Sci 69:1–10
47. Miyata T, Li D, Shiraga M et al (2006) Promoting effect of Rh, Pd and Pt noble metals to the Ni/Mg(Al)O catalysts for the DSS-like operation in CH_4 steam reforming. Appl Catal A Gen 310:97–104
48. Choudhary H, Ebitani K (2016) Hydrotalcite-supported PdPt-catalyzed aerobic oxidation of 5-hydroxymethylfurfural to 2,5-furandicarboxylic acid in water. Chem Lett 45(6):613–615
49. Cho EJ, Oh SJ (1997) Unoccupied states and the charge transfer in Cu–Pt alloys studied by bremsstrahlung isochromat spectroscopy and X-ray photoelectron spectroscopy. J Korean Phys Soc 31(2):323–328
50. Kleiman GG, Sundaram VS, Rogers JD et al (1981) X-ray photoemission spectroscopy of Pt–Cu: a canonical alloy. Phys Rev B 23(7):3177–3185
51. Yu CL, Ge QJ, Xu HY et al (2006) Effects of Ce addition on the Pt–Sn/γ-Al_2O_3 catalyst for propane dehydrogenation to propylene. Appl Catal A Gen 315:58–67
52. Redekop EA, Saerens S, Galvita VV et al (2016) Early stages in the formation and burning of graphene on a Pt/Mg(Al)O_x dehydrogenation catalyst: a temperature- and time-resolved study. J Catal 344:482–495